A First Look at Band-Differenced Angular Signatures for Cloud Detection from MISR

Larry Di Girolamo and Michael J. Wilson

***Abstract*—We present the first observational study on the potential of band-differenced angular signatures for cloud detection. A band-differenced angular signature is the reflectance difference between the blue and near-infrared channels examined as a function of view angle, and it is observed in this study from the Multi-angle Imaging SpectroRadiometer (MISR). The observed band-differenced angular signatures over a variety of scene types qualitatively compare well with previously published theoretical predictions. Examples of cloud detection in polar and desert regions using band-differenced angular signatures from MISR are shown to highlight its contribution to cloud detection in areas where traditional spectral techniques tend to perform poorly.**

***Index Terms*—Angular signature, cloud detection, Multi-angle Imaging SpectroRadiometer (MISR), polar.**

I. Introduction

THE TRADITIONAL approach to cloud detection from meteorological satellites uses spectral and spatial signatures constructed from measured radiances. They are widely recognized to have circumstances where cloud detection is difficult, such as cloud detection over snow, ice, desert, mountainous terrain, subpixel clouds, and thin clouds (typically cirrus) [1]. In order to overcome these difficulties, it may be worth exploring other aspects of the radiation field that are not commonly tapped into. These include the polarization and angular signatures of the upwelling radiation field.

Breon and Colzy [2] successfully used polarization signatures from the Polarization and Directionality of the Earth Reflectances (POLDER) instrument onboard the Advanced Earth Observing Satellite (ADEOS) for cloud detection over land. In particular, the polarization signature that they exploited was the highly polarized rainbow scattered from water clouds. Although this signature did show potential for cloud detection over a wide variety of land surfaces, it still had cloud detection difficulties for several of the traditionally difficult circumstances: 1) snow-covered land surfaces at high latitudes lacked the proper sun-view geometry to use this signature; 2) this signature is insensitive to the presence of ice clouds, which includes thin cirrus; and 3) subpixel clouds were often missed because of the course spatial resolution of the instrument ($\sim$6 km).

Angular signatures were first proposed by Di Girolamo and Davies [3] for cloud detection. They used radiative transfer simulations to show that the difference between two well-separated solar spectral channels as a function of view angle could be used for cloud detection owing to the differences in cloud and surface scattering properties and the contribution to molecular scattering above the cloud tops. They showed that this band-differenced angular signature is sensitive to thin clouds, including thin cirrus, and had the greatest potential over polar surfaces. Their study was motivated by the prospect of obtaining such multiangle, multispectral measurements from the Multi-angle Imaging SpectroRadiomter (MISR). With MISR now in orbit on the Earth Observing System (EOS) Terra satellite platform, this letter reports the first confirmation of the potential usefulness of band-differenced angular signatures for cloud detection based on observations from MISR.

Manuscript received February 16, 2003; revised May 10, 2003. This work was supported in part by the Jet Propulsion Laboratory, California Institute of Technology under Contract 1221756 and by the National Aeronautics and Space Administration under Contract ESSF/02-0000-0212.

The authors are with the Department of Atmospheric Sciences, University of Illinois at Urbana-Champaign, Urbana, IL 61801 USA (e-mail: larry@atmos.uiuc.edu; wilson@atmos.uiuc.edu).

Digital Object Identifier 10.1109/TGRS.2003.815659

II. MISR Data

Details of the MISR instrument and performance can be found in [4] and [5] respectively. In brief, the MISR instrument is in a sun-synchronous, 10:45 A.M. ECT (descending node) orbit onboard the EOS Terra satellite. It provides continuous multiangle coverage of the daylight side of the earth at nine discrete angles. This is accomplished by four fixed cameras looking forward in the along-track direction, four looking aft, and one at nadir. The surface view angles are 0° (nadir camera designated as the "An" camera), 26.1° (designated "Af" for the forward-looking along-track camera and "Aa" for the aft-looking camera), 45.6° ("Bf" and "Ba" cameras), 60.0° ("Cf" and "Ca" cameras), and 70.5° ("Df" and "Da" cameras). It takes approximately 7 min to view a given scene from all nine cameras. From its 705-km orbit, the An camera has a spatial resolution of 250 m and a swath width of 376 km. All other cameras are designed to give a cross-track resolution of 275 m with a swath width of 413 km. All cameras provide images in a pushbroom fashion in four narrow spectral bands (446, 558, 672, and 866 nm). Complete global coverage ranges from two days near the poles to nine days at the equator.

III. Comparing Theory and Observations

Di Girolamo and Davies [3] used radiative transfer simulations to propose that a band-differenced angular signature (BDAS) may be able to produce good results in cloud detection. A BDAS is simply the difference in two well-separated nonabsorbing solar spectral reflectance bands examined as a function of view angle. For MISR, the BDAS is constructed using R(446 nm) $-$ R(866 nm), where $R$is the top-of-atmosphere bidirectional reflectance factor with the spectral channels in parentheses. Di Girolamo and Davies [3] showed

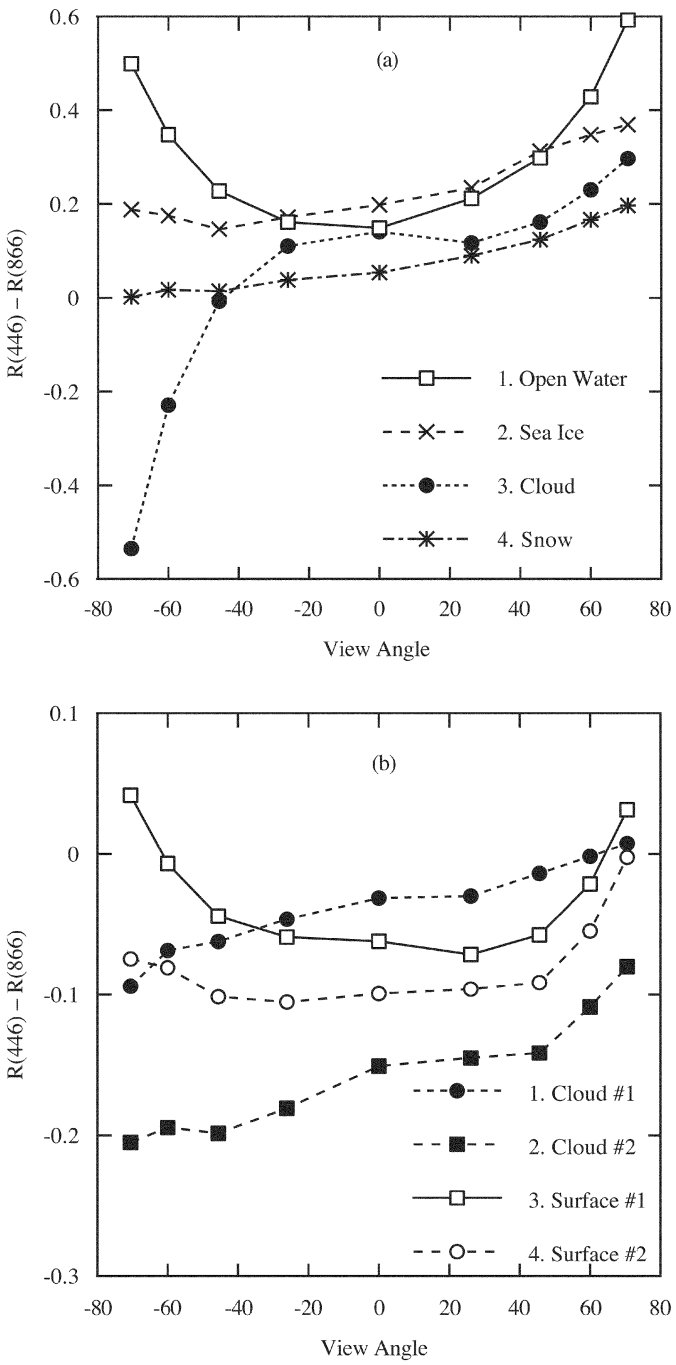

Fig. 1. Band-differenced angular signatures observed from MISR for those regions highlighted in (a) [Fig. 3(a)] and (b) [Fig. 4(a)]. Negative values of view angle are those MISR cameras that view the forward-scattered radiation.

that this band-difference as a function of view angle was often bowl-shaped for clear sky conditions. Under cloudy conditions, the BDAS shape for the cameras viewing back-scattered radiation was similar to the clear conditions. However, large departures in the BDAS shape for the cameras that view the forward-scattered radiation existed between clear and cloudy conditions. This is confirmed in the MISR observations of hundreds of different scenes examined to date. For example, Fig. 1 shows the BDAS for two scenes containing several different surface types that can be visually identified in Figs. 3 and 4. In Fig. 1(a), the BDAS for water, snow, sea ice, and

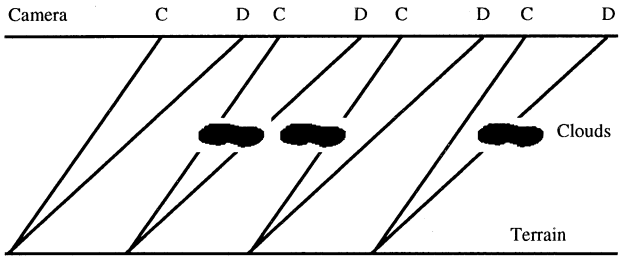

Fig. 2. Four possible clear/cloud combinations for a pair of MISR cameras whose imagery is referenced to the terrain. Each point on the terrain is viewed by the MISR C and D camera pair within ∼1 min of each other, resulting in different atmospheric paths viewed by each camera. For example, in the rightmost case in the figure, the C camera is viewing clear sky, and the D camera is viewing cloudy sky, even though both cameras are viewing the same point on the terrain.

TABLE I
TRUTH TABLE FOR THE BDAS CLOUD DETECTION OUTCOME FOR THE FOUR POSSIBLE SITUATIONS DEPICTED IN FIG. 2, WHERE MISR'S TWO MOST OBLIQUE CAMERAS THAT VIEW FORWARD-SCATTERED RADIATION ARE USED

D Camera	C Camera	BDAS
Clear	Clear	Clear
Clear	Cloud	Clear
Cloud	Clear	Cloud
Cloud	Cloud	Cloud

cloud are shown for selected regions highlighted in Fig. 3(a), while in Fig. 1(b) the BDAS for a low cloud, a high cloud, and two desert areas are shown for selected regions highlighted in Fig. 4(a). (In constructing the BDAS curves for clouds, cloud elements had to be manually tracked from camera to camera due to parallax.) These cases show that the largest differences in BDAS shape between clear and cloudy regions are for the angles that view the forward-scattered radiation. Their behavior is consistent with that predicted by [3], namely, that for MISR cameras viewing forward-scattered radiation, the BDAS has a large positive slope for clouds, a small positive or small negative slope for snow, ice, and land, and a large negative slope for water. It is this difference in BDAS slope that is exploited for cloud detection.

IV. CLOUD DETECTION USING THE BDAS

The cloud detection criterion used in [3] was the following: if the BDAS had a positive slope for all viewing directions, then the scene was cloudy. They noted that the major practical implementation problem will be camera-to-camera pixel misregistration in the presence of clouds of finite extent. The misregistration is due to parallax caused by cloud altitude and by cloud-track wind observed during the finite time between successive camera views of the same scene. Because terrain-projected radiances are used in the calculation of the BDAS, it is possible that one camera is viewing a cloud and another camera is viewing clear sky when the cameras are viewing the same point on the terrain.

We can reduce this problem for cloud detection by calculating the BDAS for a single camera pair. Consider the two most oblique MISR cameras that view the forward-scattered radiation

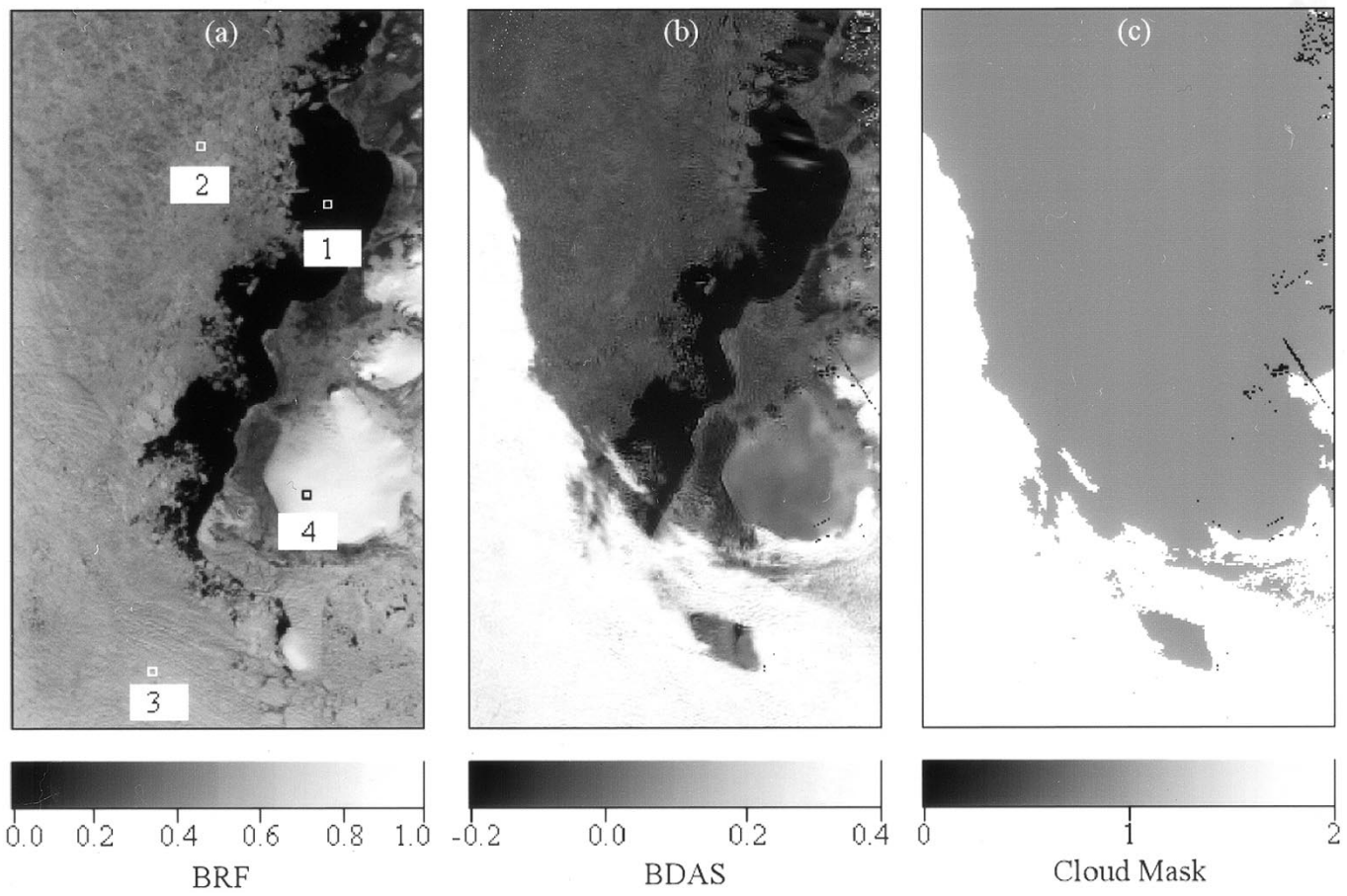

Fig. 3. (a) Top-of-atmosphere 866-nm channel bidirectional reflectance factor from the MISR An camera, (b) BDAS as defined in (1), and (c) BDAS cloud detection result, where 2 (white) represents cloud, 1 (gray) represents clear, and 0 (black) represents missing data. The labels 1, 2, 3, and 4 in (a) correspond to the regions used in producing Fig. 1(a). The scene is a subset of MISR orbit 8201, blocks 13–16, derived from version F01_0008 of the L1B2 terrain-projected radiance.

(roughly, this is the Df and Cf cameras in the northern hemisphere and the Da and Ca cameras in the southern hemisphere). These are the cameras where we expect the greatest cloud detection sensitivity based on Fig. 1. For cloud detection purposes, define the BDAS as

$$\text{BDAS} = [R(446) - R(866)]_{C\text{-cam}} - [R(446) - R(866)]_{D\text{-cam}}. \quad (1)$$

The imagery of each camera is referenced to the terrain, leading to the four possible clear/cloud combinations as depicted in Fig. 2. Table I is a truth table that represents the BDAS cloud detection outcome for the four situations depicted in Fig. 2 when we consider the BDAS behavior of clear and cloudy scenes in Fig. 1. For example, if the D camera is viewing cloud and the C camera is viewing clear, then the band-differenced slope between the C and D cameras will be a large positive value indicating cloud. Alternatively, if the D camera is viewing clear and the C camera is viewing cloud, then the band-differenced slope between the C and D cameras will be a large negative value indicating clear. Table I shows that the BDAS cloud detection outcome represents the situation within the D-camera imagery; thus, the cloud mask is assigned to the D-camera.

We have tested the BDAS for cloud detection on hundreds of MISR scenes. The quality of cloud detection was qualitatively assessed through detailed visual analysis using standard visualization software. This first-look approach has revealed excellent results over a wide range of surface and cloud conditions, especially for cirrus clouds as predicted in [3]. A discussion on global application and validation of the BDAS for cloud detection using MISR data are given in the next section. Here, we simply give two examples that highlight the potential that the BDAS has for cloud detection. We choose to show two scenes that offer great difficulties to modern spectral cloud detection approaches. To be sure, we visually compared our cloud masks to that derived from the EOS Terra Moderate Resolution Imaging Spectroradiometer (MODIS) operational cloud mask [6] (Version 3) and chose scenes where the MODIS cloud mask failed to produce reasonable results, which turned out not to be thin cirrus cases (MODIS results are not shown here due to space limitations, but can be obtained from the Goddard Distributed Active Archive Center). These two scenes are shown in Figs. 3 and 4. Fig. 3(a) shows MISR imagery collected over the Arctic Ocean north of Russia (centered at 80.7°N, 99.9°E) on July 3, 2001. The imagery shows a mix of scene types: open water, sea ice, snow-covered land (Komsomolets Island), and cloud. The cloud toward the lower left in Fig. 3(a) is difficult to see since

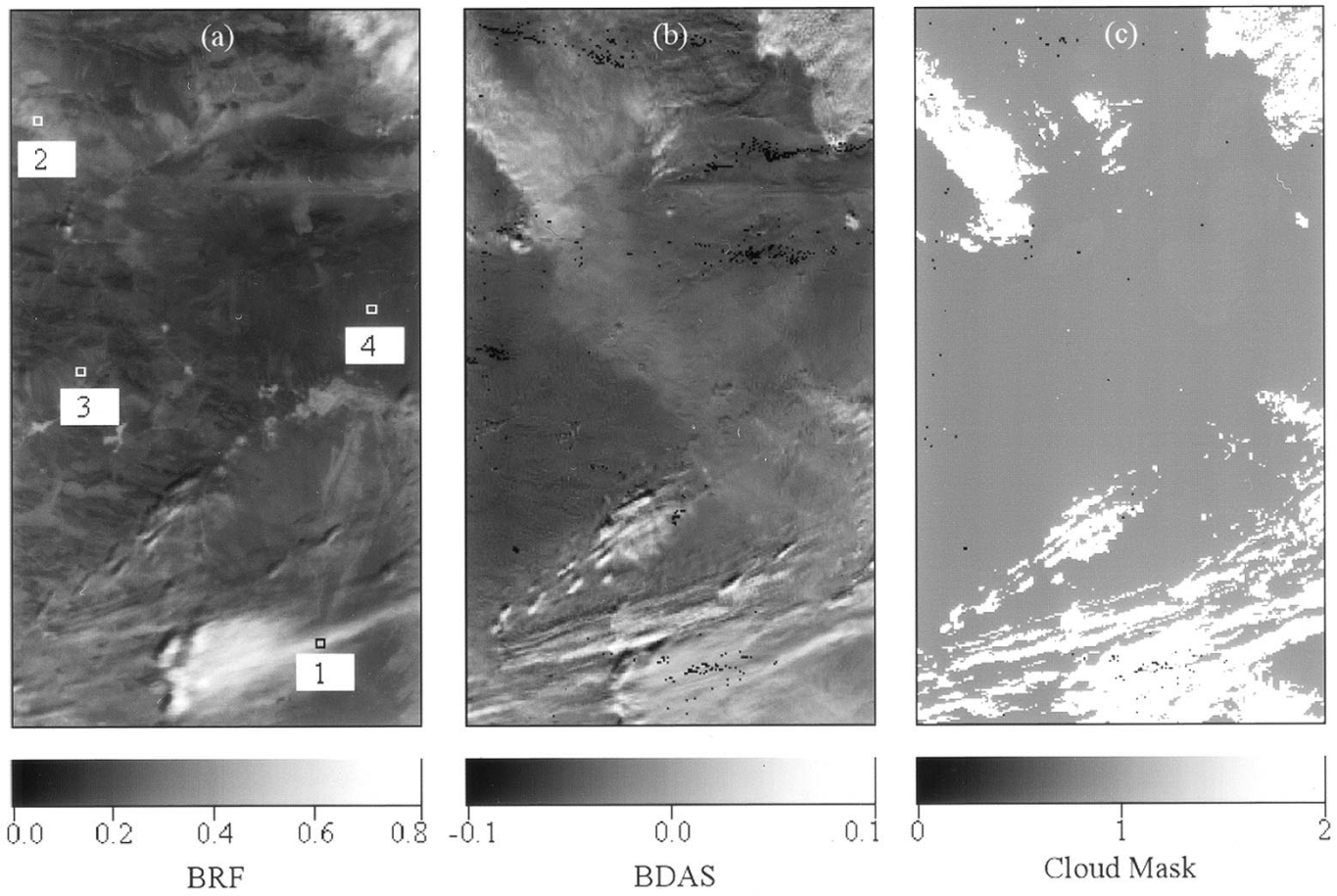

Fig. 4. Same as Fig. 3, except that the scene is a subset of MISR orbit 6565, blocks 50–53, derived from version F01_0014 of the L1B2 terrain-projected radiance. The labels 1, 2, 3, and 4 in (a) correspond to the regions used in producing Fig. 1(b).

it is a low-altitude (MISR stereoscopic heights ∼600 m), optically thin (since sea ice features are visible through the cloud) stratus cloud. Fig. 4(a) shows MISR imagery collected over the Gobi Dessert (centered on 42.7°N, 100.0°E), wedged between the Altai and Qilian Mountains, on March 13, 2001. The imagery shows a variety of different barren desert surfaces over flat and rugged terrain, as well as some clouds.

The BDAS, as defined in (1), for these two scenes are shown in Figs. 3(b) and 4(b). (Since the BDAS is calculated using terrain-projected BRFs, some missing data is inevitable in high relief areas.) These figures show that it is much easier to discriminate clouds from the surface using a single BDAS threshold over the entire scene as compared to using a single reflectance value over Figs. 3(a) and 4(a). Fig. 3(c) shows the cloud mask when a single BDAS threshold of 0.17 is applied to the entire scene in Fig. 3(b). The results are visually very good. There are two small, thin clouds above region 1 in Fig. 3(a) that can only be seen in Fig. 3(b). These two clouds fall below the threshold of 0.17 and were, thus, not detected in the cloud mask [Fig. 3(c)]. Lowering the threshold to detect the two small clouds would have led to some clear land pixels being labeled as cloudy. This problem can be reduced by making thresholds depend on surface type (see Section V). Fig. 4(c) shows the cloud mask when a single BDAS threshold of 0.00 is applied to the entire scene in Fig. 4(b). This scene was one of the most difficult scenes that we examined. Yet, the results are still visually good, with perhaps one exception. More difficult to see are the clouds or heavy dust clouds in the upper left of the image. Close examination of a true color 250-m MISR image of the feature labeled as "2" in Fig. 4(a) has revealed some ambiguity on whether the feature is a water cloud or a dust cloud, based on spectral and spatial examination of both MISR and MODIS data. The MODIS operational algorithm labeled it a cloud. However, the MODIS algorithm was designed to detect clear scenes, so it tends to detect more false positive clouds. MISR stereoscopic heights place it at approximately 1.3 km. Results on other known elevated dust scenes have revealed an inability to discriminate between cloud and thick dust, revealing a potential limitation of the BDAS approach taken here for cloud detection. However, Fig. 1(b) suggests that an examination of the absolute difference in the band-difference between Clouds 1 and 2 may be used to discriminate thick dust from cloud. This is the subject of future work.

V. Discussion

We have confirmed in this letter that the shape of the band-differenced angular signature from MISR observations qualitatively matches the theoretical predictions given in [3] and that it may have great potential for cloud detection, including cloud detection in traditionally difficult circumstances. It is important to note, however, that we have only demonstrated its po-

tential for cloud detection on a scene-by-scene basis by tuning a single BDAS threshold for individual MISR scenes. Its potential for global, automated cloud detection has not yet been demonstrated, as this requires a globally applicable threshold dataset that depends on sun-view geometry and surface type. This can only be achieved once the MISR production software for cloud detection becomes fully operational (anticipated to be in place in 2004). The currently planned MISR algorithm for global automated cloud detection using the BDAS is given in [6]. It will be assessed for quality using a combination of comparisons with ground-based data, the MODIS operational cloud mask, other independent MISR cloud masks (RCCM and SDCM in [7]), and visual inspections.

ACKNOWLEDGMENT

The authors would like extend thanks to the four anonymous reviewers for the time and care they put into reviewing the original manuscript.

REFERENCES

[1] W. B. Rossow, "Measuring cloud properties from space: A review," *J. Clim.*, vol. 2, pp. 201–213, 1989.

[2] F.-M. Breon and S. Colzy, "Cloud detection from the Spaceborne POLDER instrument and validation against surface synoptic observations," *J. Appl. Meteorol.*, vol. 38, pp. 777–785, 1999.

[3] L. Di Girolamo and R. Davies, "A band-differenced angular signature technique for cirrus cloud detection," *IEEE Trans. Geosci. Remote Sensing*, vol. 32, pp. 890–896, July 1994.

[4] D. J. Diner, J. C. Beckert, T. H. Reilly, C. J. Bruegge, J. E. Conel, R. A. Kahn, J. V. Martonchik, T. P. Ackerman, R. Davies, S. A. W. Gerstl, H. R. Gordon, J.-P. Muller, R. B. Myneni, P. J. Sellers, B. Pinty, and M. Verstraete, "Multi-angle Imaging SpectroRadiometer (MISR) instrument description and experiment overview," *IEEE Trans. Geosci. Remote Sensing*, vol. 36, pp. 1072–1087, July 1998.

[5] D. J. Diner, J. C. Beckert, G. W. Bothwell, and J. I. Rodriguez, "Performance of the MISR instrument during its first 20 months in earth orbit," *IEEE Trans. Geosci. Remote Sensing*, vol. 40, pp. 1449–1466, July 2002.

[6] S. A. Ackerman, K. Strabala, W. P. Menzel, R. A. Frey, C. C. Moeller, and L. E. Gumley, "Discriminating clear sky from clouds with MODIS," *J. Geophys. Res.*, vol. 103, pp. 32 141–32 158, 1998.

[7] D. J. Diner, R. Davies, L. Di Girolamo, A. Horvath, C. Moroney, J.-P. Muller, S. R. Paradise, D. Wenkert, and J. Zong, "MISR Level 2 cloud detection and classification algorithm theoretical basis," Jet Propulsion Lab., Pasadena, CA, JPL Tech. Doc. D-11399, Rev. D, 1999.